ACS OMEGA

http://pubs.acs.org/journal/acsodf

Article

Apple-like Zinc-Oxide Mesocrystals as Robust and Versatile Photocatalysts for Efficient Degradation of Eight Different Organic Dyes

Huixia He, Caihong Fu, Wenyu Wei, Jianrui Ma, Xiaoyu Guo, and Jianxi Xiao*

Cite This: *ACS Omega* 2022, 7, 409–418

Read Online

ACCESS | Metrics & More | Article Recommendations | Supporting Information

ABSTRACT: The discovery of efficient photocatalysts is a promising key approach to solve the environmental crisis caused by hazardous organic dyes. Herein, we have for the first time created ZnO mesocrystals with a novel apple-like morphology. We have developed a one-pot biomineralization route to synthesize ZnO nanostructures at room temperature by using the rod-like protein collagen as the template. The shape of ZnO mesocrystals can be conveniently tuned from fusiform-like and kiwi-like to orange-like, apple-like, and snack-like structures. The apple-like ZnO mesocrystals show a significantly better photodegradation efficiency than the commercial ZnO powder as well as other nanostructured ZnO materials for both rhodamine B (RhB) and methyl orange (MO). Furthermore, the apple-like zinc-oxide mesocrystals can degrade all of the tested eight different types of organic dyes (RhB, rhodamine 6G, methylene blue, Coomassie brilliant blue R250, BPB, MO, Li Chunhong S, and carmine) simply under the exposure of sunlight, demonstrating their superior photodegradation prowess, environmental amiability, and energy-saving features. The novel robust and versatile photocatalyst has greatly advanced our abilities for the elimination of organic dyes. The green, one-pot strategy provides a convenient method for the construction of novel metal-oxide nanostructures with promising applications in environmental protection.

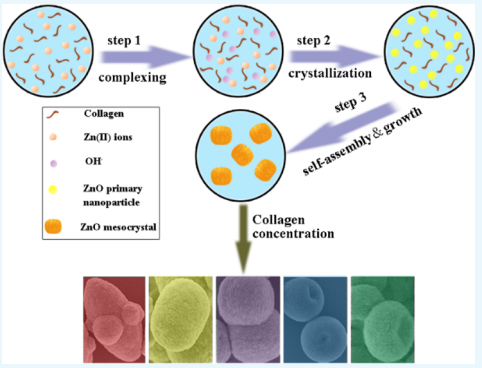

INTRODUCTION

Hazardous organic pollutants from a wide range of industries such as leather and textile have caused alarming environmental deterioration.[1−3] Organic dyes are among the predominant pollutants, and they are well known for their resistance to degradation under ambient conditions due to their chemical structure and stability.[4] About a half of these dyes belong to the Azo dye family including methyl orange (MO), which share the chromophore (−N═N−) in their molecular structure.[5−7] The Azo dyes have been reported to cause carcinogenic, genotoxic, and mutagenic hazards on living beings.[4,6,8] Rhodamines are another popular type of organic dyes found in the effluents produced by cosmetic and pharmaceutical factories. Therefore, it is of top priority to find an efficient solution for the remediation of dye contamination in waste water.

A variety of chemical and physical methods such as chemical precipitation and adsorption have been established for the treatment of organic dyes.[9−13] However, these conventional approaches often suffered from severe drawbacks such as incomplete degradation, secondary pollution, and high operational cost.[14−16] Photocatalysis has thus attracted increasing attention as a promising technique for the degradation of organic dyes in contaminated water due to its high efficiency and low cost.[17−20] Metal semiconductor materials have advantages such as low energy consumption and nontoxicity, and they have recently been investigated as potential photocatalysts to remove dye pollutants.[21−23]

As an important n-type semiconductor, zinc oxide (ZnO) has a room-temperature wide band gap of 3.37 eV and a high excitation binding energy of 60 meV.[24−26] Zinc-oxide nanoparticles have shown exceptional ability to utilize UV and/or visible light, leading to the production of electron−hole pairs.[27] The interaction between the electron/hole and O_2/H_2O results in the generation of free radicals $\cdot O^{2-}$ and ·OH, which are capable of complete degradation of organic dyes.[28−34] Compared with other reported metal semiconductors, ZnO nanoparticles have shown higher efficiency in the photocatalytic degradation of some organic dyes.[35,36]

Extensive efforts have been devoted to synthesize zinc oxide with well-ordered nanostructures. Different techniques including electrochemical deposition, sol−gel, hydrothermal, and biological methods have been explored, and a broad range of

Received: August 31, 2021
Accepted: December 9, 2021
Published: December 23, 2021

https://doi.org/10.1021/acsomega.1c04782
ACS Omega 2022, 7, 409−418

hierarchical structures such as nanospindles, nanopropellers, nanoflowers, nanoplants, nanocages, nanodisks, nanorings, hollow microspheres, and peanut-like, doughnut-like, and tower-like structures have been achieved.[37−46] It has been proposed that the morphologies and sizes of ZnO nanoparticles play a determinant role in their degradation efficiency.[47] The discovery of novel nanostructures is essential for the development of a robust ZnO photocatalyst.

Biomineralization is a ubiquitous strategy adopted by living beings to synthesize inorganic crystals, while the unique triple helical protein collagen has been selected as one of the most important templates for the fabrication of nanostructured mesocrystals (e.g., bones, cartilage, and teeth) in animals.[48,49] Herein, we have for the first time reported the production of hierarchical apple-like ZnO mesocrystals. Collagen has been established as a robust template to finely tune the nanostructures of ZnO under mild biomineralization conditions. The novel apple-like ZnO mesocrystals displayed superior photocatalytic degradation capability against all of the eight tested organic dyes, with great potential in environmental applications.

RESULTS AND DISCUSSION

Characterization of Zinc-Oxide Nanostructures. The crystal type of the nanomaterials prepared by collagen-templated biomineralization ([collagen] = 0.2 wt % and [Zn (II)] = 0.1 M) for 8 days at room temperature was evaluated by the X-ray diffraction (XRD) technique (Figure 1). The

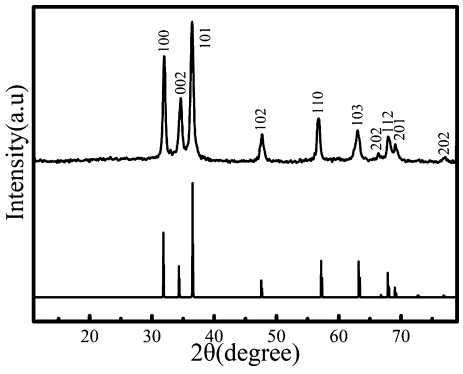

Figure 1. XRD pattern of the zinc-oxide samples obtained after 8 days of collagen-templated biomineralization at room temperature ([collagen] = 0.2 wt %, [Zn (II)] = 0.1 M). The standard XRD pattern (zinc oxide, JCPDS no. 36-1451) is shown beneath the plot.

diffraction profile was completely matched with the standard XRD pattern of pure ZnO crystal (zinc oxide JCPDS no. 36-1451) (Figure 1). The chemical composition of the prepared nanomaterials was analyzed by X-ray photoelectron spectroscopy (XPS) (Figure S1). The observed XPS peaks corresponding to C 1s and N 1s indicated the presence of collagen in the nanomaterials, while the two strong peaks assigned to Zn 2p 1/2 and Zn 2p 3/2 suggested the production of ZnO. The XRD and XPS results indicated that the nanomaterials produced by collagen-templated biomineralization were pure ZnO without any other phases.

The morphology of zinc-oxide samples was characterized by field emission scanning electron microscopy (FESEM) and transmission electron microscopy (TEM). Zinc-oxide mesocrystals were prepared by 8 days of collagen-templated biomineralization with the concentration of collagen as 0.2 wt % and that of Zn (II) as 0.1 M at room temperature. The SEM images showed a uniform apple-like geometry of 4 μm × 2.5 μm in the long axis and short axis (Figure 2a). A closer observation indicated that the apple-like mesocrystal had a rough surface, and it consisted of primary nanoparticle units (Figure 2b). The TEM image further confirmed that the zinc-oxide mesocrystals were assembled by primary nanoparticles in orientation (Figure 2c). The selected area electron diffraction (SAED) pattern obtained from the edge of the sample showed a typical single-crystal spot pattern, indicating that the primary zinc-oxide nanoparticles were assembled in quite an oriented way (Figure 2d). The high-resolution transmission electron microscopy (HRTEM) image showed the characteristic (101) lattice spacing (0.26 nm), demonstrating the highly ordered arrangement of the nanoparticles (Figure 2e). The high-angle annular dark-field scanning TEM (HAADF-STEM) image showed the porous nature of the apple-like zinc-oxide mesocrystals, suggesting that the primary zinc-oxide nanoparticles gradually assemble to form mesocrystals with hierarchical nanostructures (Figure 2g). The energy-dispersive X-ray spectroscopy (EDX) spectrum indicated the presence of elements C, Zn, and O, demonstrating the inclusion of collagen in the ZnO particles (Figure 2f). Elemental mapping results by EDX indicated that the elements C, O, and Zn were homogeneously distributed throughout the mesocrystal, further confirming the presence of collagen in the zinc-oxide mesocrystals (Figure 2h).

Thermogravimetric analysis (TGA) was carried out to examine the content of the collagen in the zinc-oxide mesocrystals (Figure S2). There were two steps for the weight loss. The first step was water elimination, which occurred at temperatures below 200 °C. When the temperature was between 200 and 700 °C, the second step corresponding to the thermal decomposition of collagen took place (Figure S2). When the addition of collagen in the reaction mixture was 0.01 and 0.2 wt %, the content of collagen in the final zinc-oxide mesocrystal was estimated to be 2.6 and 8.3 wt %, respectively. It indicated that collagen played a crucial role in the formation process of ZnO nanostructures, and a significant amount of collagen was packed within the zinc-oxide mesocrystals. In addition, the nitrogen adsorption/desorption isotherms of the apple-like zinc-oxide mesocrystal were obtained (Figure S3). By using the Barrett−Joyner−Halenda (BJH) model, its specific surface area was calculated as 93.54 m^2/g with an average pore size of approximately 10 nm, indicating the porous nature of the zinc-oxide mesocrystals (Figure S3). All these results demonstrated that the mild biomineralization process using collagen as the biotemplate can produce zinc-oxide mesocrystals with highly ordered hierarchical structures.

Time-dependent Growth of the Apple-like Zinc-Oxide Mesocrystals. In order to decipher the formation mechanism of apple-like ZnO mesocrystal, FESEM and XRD techniques were employed to monitor the time-dependent evolution process (Figures 3, 4). At the initial stage, the mixture of collagen and zinc nitrate under alkali condition led to nanoneedle-like particles after 10 min of incubation (Figure 3a−c). They started to form apple-like particles after 1 h of incubation (Figure 3d−f). The apple-like nanostructure became the dominant product after 4 days of incubation (Figure 3g,h). When the reaction was extended to 7 days, uniform apple-like particles were observed (Figure 3i).

Meanwhile, the nanomaterials obtained at different times of incubation (10 min, 15 min, 30 min, 1 h, 12 h, 2 d, 4 d, 6 d,

https://doi.org/10.1021/acsomega.1c04782
ACS Omega 2022, 7, 409−418

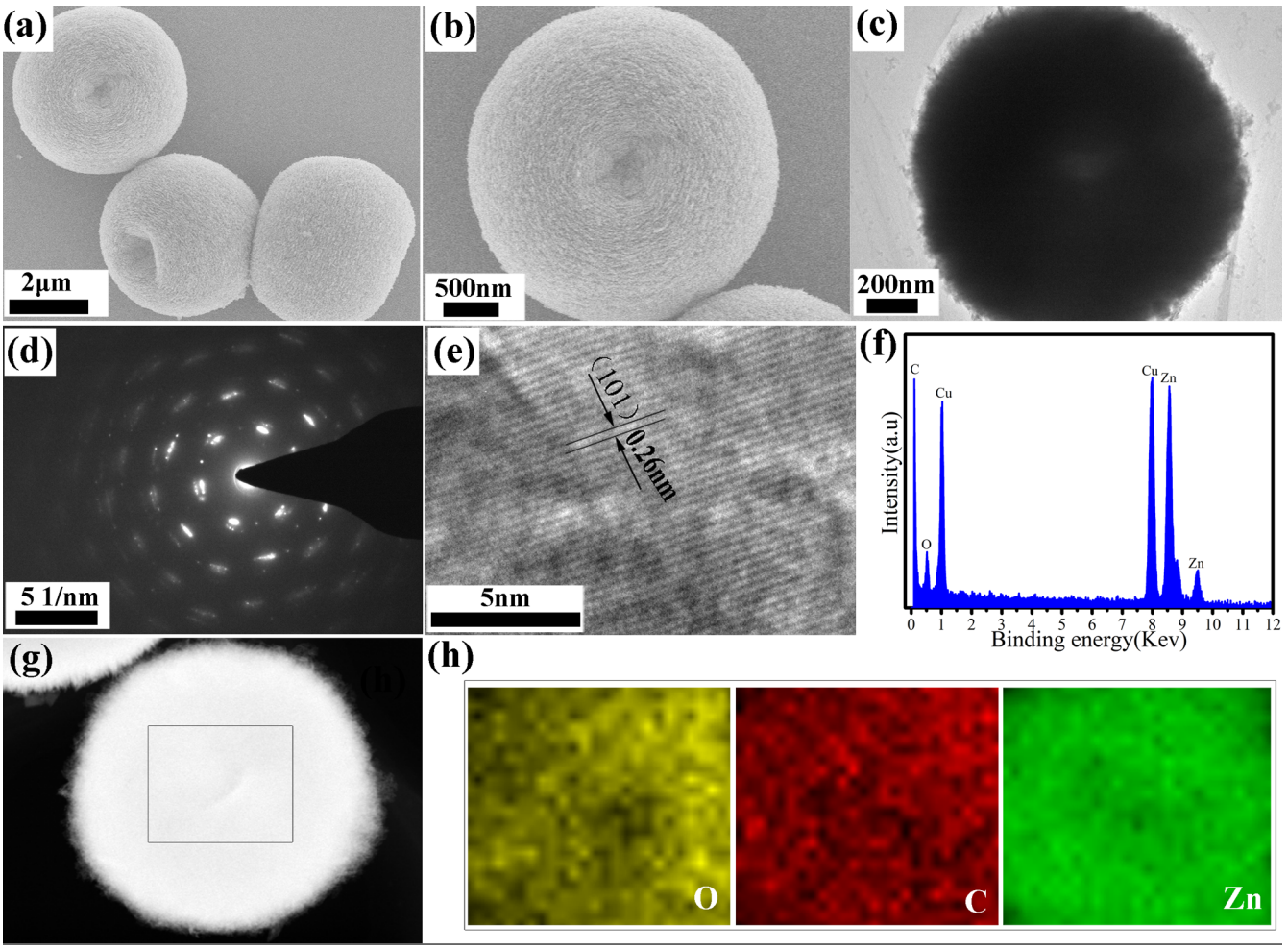

Figure 2. (a,b) FESEM images of the apple-like zinc-oxide mesocrystal obtained after 8 days of collagen-templated biomineralization at room temperature ([collagen] = 0.2 wt %, [Zn^{2+}] = 0.1 M); (c) TEM image, (d) SAED pattern, and (e) HRTEM image (e) of the ZnO mesocrystal; (f) EDX spectrum of the apple-like ZnO mesocrystal, where the signals of Cu are generated from the Cu grid support film; (g) HAADF-STEM image of the apple-like zinc-oxide particles; (h) EDS mapping images of O, C, and Zn for the square region of the ZnO particles in (g).

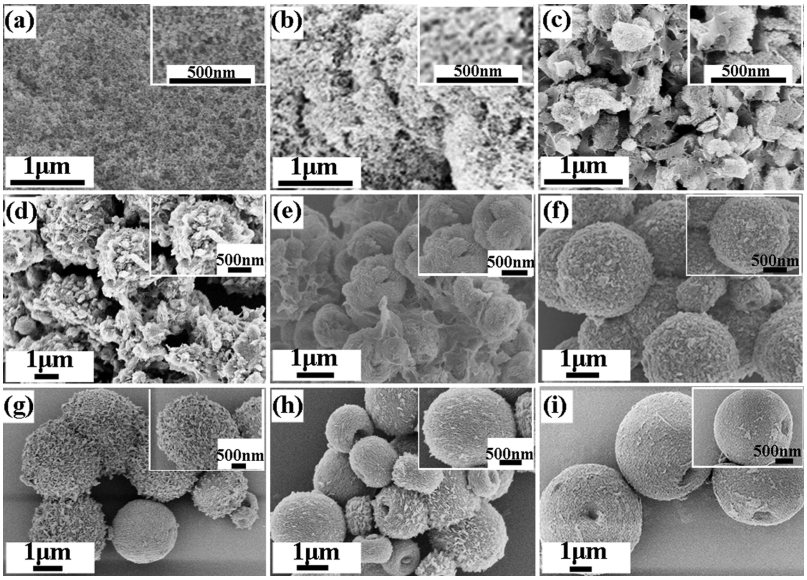

Figure 3. FESEM images of the apple-like ZnO mesocrystal obtained via collagen-templated biomineralization at room temperature ([collagen] = 0.2 wt %, [Zn(II)] = 0.1 M) at different incubation times: (a) 10 min; (b) 15 min; (c) 30 min; (d) 1 h; (e) 12 h; (f) 2 days; (g) 4 days; (h) 6 days; (i) 7 days.

https://doi.org/10.1021/acsomega.1c04782
ACS Omega 2022, 7, 409−418

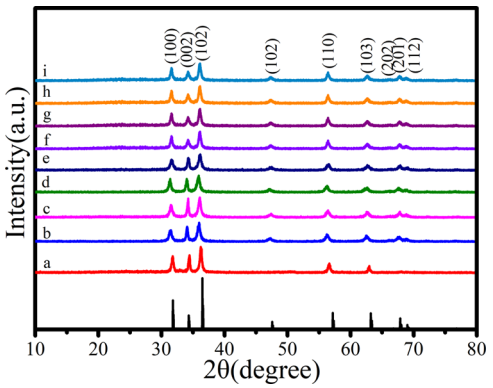

Figure 4. XRD patterns of the apple-like ZnO mesocrystal obtained via collagen-templated biomineralization at room temperature ([collagen] = 0.2 wt %, [Zn (II)] = 0.1 M) at different incubation times: (a) 10 min; (b) 15 min; (c) 30 min; (d) 1 h; (e) 12 h; (f) 2 days; (g) 4 days; (h) 6 days; (i) 7 days. The standard XRD pattern (zinc oxide, JCPDS no. 36-1451) is shown beneath the plot.

and 7 d) displayed the same XRD pattern assigned to a pure zinc-oxide crystal (Figure 4). It suggested that the mixture formed primary zinc-oxide crystals at the initial stage and maintained the same crystal phase during the growth of mesocrystals. Importantly, it is noteworthy that the exposure of the (002) crystal face was relatively high within the first hour, while the exposure of the (100) crystal face got much increased after 12 h of incubation (Figure 4). The reduction in D_{002} suggested that collagen controlled the crystalline morphology by preferential adsorption on the basal plane. All results indicated that the mild biomineralization condition resulted in zinc-oxide crystals in a short time, while it took a long process to form an exquisite apple-like morphology, and collagen played a predominant role through interaction with preferential crystal faces.

Critical Role of Collagen in Biomineralized ZnO Nanostructures. In order to explore the role of collagen in the biomineralization, the morphologies of zinc-oxide mesocrystals were examined under a range of collagen concentrations from 0 to 0.5 wt % while maintaining a constant Zn (II) concentration of 0.1 M (Figure 5). When no collagen was added in the reaction mixture, disordered particles were observed (Figure 5a). With only a tiny amount of collagen (0.01 wt %), relatively uniform fusiform-like ZnO mesocrystals were formed (Figure 5b). With the collagen concentration increased to 0.05 w %, kiwi-like ZnO mesocrystals were formed (Figure 5c). When the concentration of collagen was further increased to 0.1 wt %, the shape of zinc-oxide mesocrystals changed to an orange-like structure and formed a uniform apple-like structure at 0.2 wt % (Figure 5d,e). When the concentration of collagen reached 0.5 wt %, zinc-oxide mesocrystals formed a dominantly snack-like shape (Figure 5f). The remarkable dependence of the morphologies of zinc-oxide mesocrystals on the concentration of collagen suggested that collagen could finely modulate the ZnO nanostructures.

A possible mechanism has been proposed for the biomineralized synthesis of various ZnO nanostructures (Scheme 1). At the initial stage, the addition of zinc nitrate into collagen solution leads to the formation of the Zn(II)-collagen complexes triggered by the interaction of the zinc ions with the polar groups in collagen. Then, the addition of sodium hydroxide immediately drives the formation of primary ZnO nanoparticles. Third, these primary nanoparticles further

Scheme 1. Illustration of the Critical Role of Collagen in the Modulation of Zinc-Oxide Nanostructures

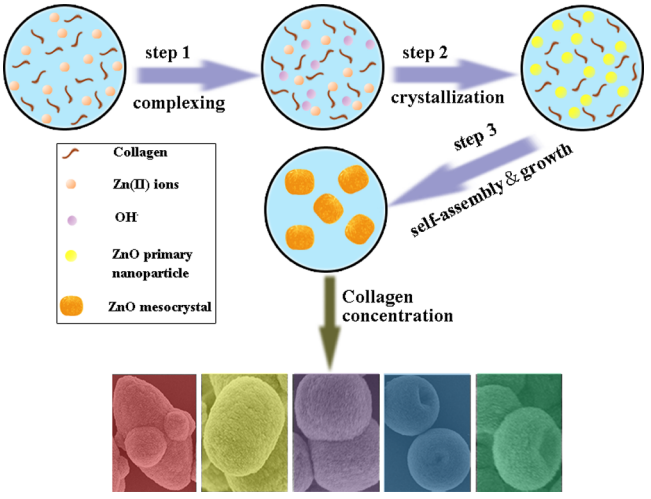

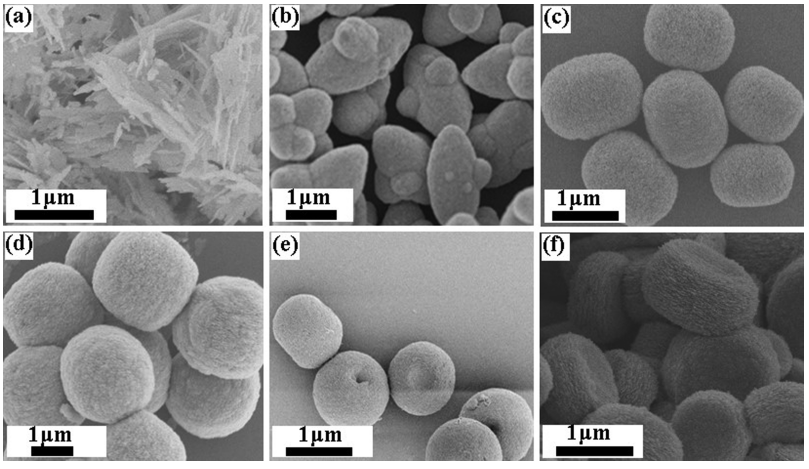

Figure 5. FESEM images of the as-prepared zinc-oxide mesocrystals obtained after 8 days of biomineralization at room temperature with a constant concentration of Zn(II) (0.1 M) and varying concentrations of collagen: (a) 0, (b) 0.01, (c) 0.05, (d) 0.1, (e) 0.2, and (f) 0.5 wt %.

https://doi.org/10.1021/acsomega.1c04782
ACS Omega 2022, 7, 409−418

assemble into larger nanoparticles and finally form various mature nanostructures. Collagen provides a unique rod-like template to mediate the assembly, while the morphologies of the assemblies could be conveniently mediated by adjusting the collagen concentration.

Effect of Zinc Ions on ZnO Nanostructures. In order to evaluate the role of Zn(II) in the biomineralization, the morphologies of zinc-oxide mesocrystals were characterized under different Zn(II) concentrations ranging from 0.01 to 0.4 M while keeping a constant collagen concentration of 0.2 wt % (Figure S4). When the Zn(II) concentration was 0.01 and 0.05 M, the zinc-oxide mesocrystals displayed star-like and plane-like shapes, respectively (Figure S4a,b). When the Zn(II) concentration was increased to 0.2 and 0.4 M, the zinc-oxide mesocrystals formed a sheet-like structure (Figure S4c,d). These results indicated that Zn(II) played a critical role in modulating the morphologies of ZnO mesocrystals in the biomineralization process.

Photodegradation Performance of Zinc-Oxide Nanostructures. Zinc oxide has been well known as a semiconductor photocatalyst to catalyze the photodegradation of organic contaminants in aqueous solutions.[50,51] As potential applications, the photodegradation performance of the as-prepared zinc-oxide mesocrystals using rhodamine B (RhB) as the substrate was examined (Figure 6). 10 mg of apple-like ZnO mesocrystals was dispersed in 100 mL of RhB aqueous solution (12 mg/L), and the mixture was exposed to ultraviolet light irradiation for different periods of time. Before the irradiation, UV−vis spectra of RhB showed a strong absorption at 553 nm (Figure 6a). As the exposure time was increased, the characteristic absorption peak at 553 nm got decreased rapidly. After 180 min of exposure, the absorption at 553 nm became almost zero, indicating that all RhB had been degraded (Figure 6a). The graphs of the mixture showed a similar phenomenon, where its red color became weaker and finally disappeared, visually confirming the successful degradation of RhB (Figure 6a).

The effect of morphology on the photodegradation efficiency of zinc-oxide mesocrystals was further investigated (Figure 6b). Commercial ZnO samples without any ordered structure were used as the control. All forms of ZnO particles showed some capability to degrade RhB, while the degradation efficiency clearly depended on the morphology (Figure 6b). After 180 min, the commercial ZnO had degraded 39.1% of RhB. In contrast, ZnO mesocrystals with fusiform-like, kiwi-like, orange-like, and snack-like shapes had degraded 59.6, 89.2, 91.7, and 93.5% of RhB, respectively. It indicated that all biomineralized ZnO mesocrystals with an ordered geometry possessed much stronger photocatalytic power. Most importantly, the apple-like ZnO mesocrystals showed the highest degradation efficiency of RhB (98.8%) (Figure S5).

The photodegradation performance of the as-prepared zinc-oxide mesocrystals using MO as the second substrate was investigated (Figure 7). 10 mg of apple-like ZnO mesocrystals was dispersed in 100 mL of MO aqueous solution (12 mg/L),

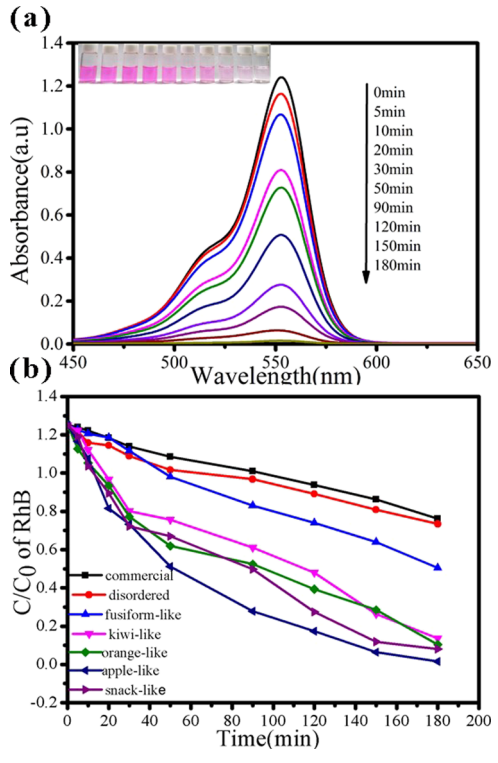

Figure 6. (a) Photocatalytic degradation of RhB by apple-like ZnO mesocrystals. UV−vis spectra of the RhB solution mixed with apple-like ZnO mesocrystals after different exposure times; inset: corresponding photographs of the RhB solutions. (b) Photocatalytic degradation of RhB under UV light irradiation in the presence of ZnO samples with different morphologies. The UV−vis absorption intensity at 553 nm as a function of exposure time for different ZnO samples.

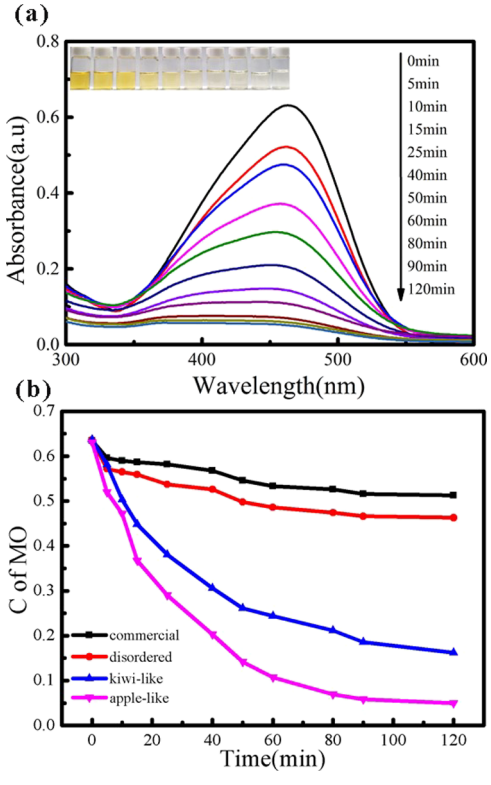

Figure 7. (a) Photocatalytic degradation of MO by apple-like ZnO mesocrystals. UV−vis spectra of the MO solution mixed with apple-like ZnO mesocrystals after different exposure times; inset: corresponding photographs of the MO solutions. (b) Photocatalytic degradation of MO under UV light irradiation in the presence of ZnO samples with different morphologies. The UV−vis absorption intensity at 464 nm as a function of exposure time for different ZnO samples.

https://doi.org/10.1021/acsomega.1c04782
ACS Omega 2022, 7, 409−418

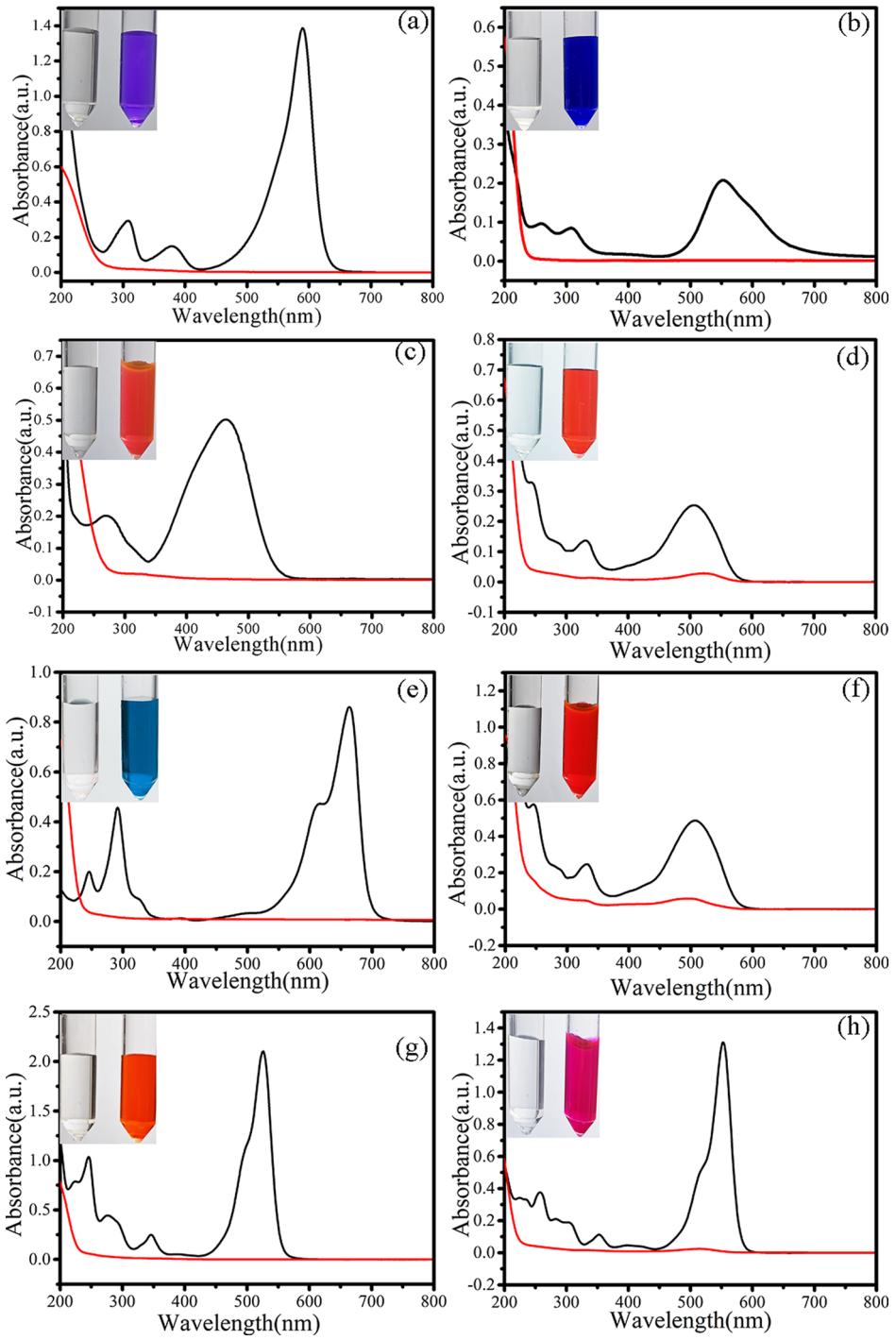

Figure 8. Photocatalytic degradation of different organic dyes [(a) BPB, (b) Coomassie brilliant blue R250, (c) MO, (d) Li Chunhong S, (e) methylene blue, (f) carmine, (g) rhodamine 6G, and (h) RhB] by apple-like ZnO mesocrystals. UV−vis spectra of each dye solution treated (red) and untreated (black) by apple-like ZnO mesocrystals; inset: corresponding photographs of each dye solution treated (left) and untreated (right) by apple-like ZnO mesocrystals.

and the mixture was exposed to ultraviolet light irradiation for different periods of time. Before irradiation, the UV−vis spectra of MO showed a strong absorption at 464 nm (Figure 7a). As the exposure time was increased, the characteristic absorption peak at 464 nm got decreased rapidly. After 120 min of exposure, the absorption at 464 nm became almost zero, indicating all MO had been degraded (Figure 7a). The graphs of the mixture showed a similar phenomenon, where its red color became weaker and finally disappeared, visually confirming the successful degradation of MO (Figure 7a). The degradation efficiency also depended on the morphology of ZnO, while ZnO mesocrystals with kiwi-like and apple-like shapes had degraded 74.7 and 96.9% of MO. These results indicated that apple-like zinc-oxide mesocrystals were the best photocatalyst for both RhB and MO.

The photodegradation performance of the apple-like zinc-oxide mesocrystals was evaluated using a broad variety of organic dyes including RhB, rhodamine 6G, methylene blue,

https://doi.org/10.1021/acsomega.1c04782
ACS Omega 2022, 7, 409−418

Coomassie brilliant blue R250, BPB, MO, Li Chunhong S, and carmine under sunlight (Figure 8). 10 mg of apple-like ZnO mesocrystals was dispersed in 100 mL of each organic dye solution (12 mg/L), and the mixture was exposed to sunlight for 2 days. It is worth noting that all tested organic dyes were completely degraded by apple-like zinc-oxide mesocrystals, demonstrating apple-like zinc-oxide mesocrystals as a robust and versatile photocatalyst for organic dyes. Furthermore, besides ultraviolet light, the apple-like zinc-oxide mesocrystals can degrade all dyes simply under the exposure of sunlight, demonstrating the superior photodegradation prowess, environmental amiability, and energy-saving features.

Previous studies have shown that ZnO mesocrystals with a well-ordered morphology displayed excellent photodegradation capability.[42,46,52] It was suggested that the photocatalytic degradation of organic dyes occurred in an indirect pathway involving hydroxyl radicals as the oxidizing intermediates.[29,53] When zinc oxide was irradiated with ultraviolet light, the conduction band electrons and valence holes were generated on the surface of the zinc-oxide nanoparticles.[54] The vacancy could react with the water adhering to the surface of the zinc oxide to form a highly reactive hydroxyl radical, which had strong oxidation capacity and could degrade organic dyes.[55]

CONCLUSIONS

The development of efficient photocatalysts is essential for the remediation of organic dyes in polluted water. To our knowledge, a novel apple-like nanostructure has been for the first time achieved for zinc-oxide mesocrystals. Collagen, the main protein template for the production of mineralized tissues in human beings, has been utilized to assist the synthesis of ZnO mesocrystals via a one-pot biomineralization route at room temperature. XRD and XPS characterizations demonstrated that pure ZnO crystal was produced via this collagen-templated biomineralization process, while the SEM and TEM images indicated a well-ordered apple-like geometry for the as-prepared ZnO mesocrystals. The TGA experiments further confirmed the presence of significant collagen in the ZnO mesocrystals. As the concentration of collagen got increased, the shape of ZnO mesocrystals changed from fusiform-like to kiwi-like, orange-like, apple-like, and finally snack-like. Collagen has been demonstrated as a determinant factor in modulating the morphologies of ZnO mesocrystals.

The photodegradation performance of the as-prepared ZnO mesocrystals of various nanostructures were tested using two substrates RhB and MO. Notably, the apple-like ZnO mesocrystals showed much higher photodegradation efficiency than the commercial ZnO powder as well as other nanostructured ZnO materials (fusiform-like, kiwi-like, orange-like, and finally snack-like) for both RhB and MO. Remarkably, the novel apple-like ZnO mesocrystals demonstrated superior photocatalytic degradation capability against all of the eight tested organic dyes (BPB, Coomassie brilliant blue R250, MO, Li Chunhong S, methylene blue, carmine, rhodamine 6G, and RhB). The discovery of the green, robust, and versatile photocatalyst has greatly advanced our capabilities for the remediation of organic dyes. The energy-saving, environmentally friendly, one-pot strategy provides a convenient method for the fabrication of novel metal-oxide nanostructures, which have great potential in the construction of powerful semiconductor photocatalysts with promising applications in environmental protection.

EXPERIMENTAL SECTION

Preparation of Recombinant Collagen. Recombinant collagen was expressed in *Escherichia coli* (*E. coli*) *BL21* strain as previously described.[56] Cells were grown in LB medium with 100 μg/mL ampicillin at 37 °C, and 1 mM isopropyl beta-D-thiogalactopyranoside was added to initiate protein expression at 25 °C when OD_{600nm} reached 0.8. Cells were disrupted by sonication, and the supernatant was harvested. Crude proteins were purified on a Ni-NTA-Sepharose column using the elution buffer (20 mM sodium phosphate buffer pH 7.4, 500 mM NaCl, 500 mM imidazole). Recombinant collagen was obtained from the purified protein by trypsin digestion to remove the folding domain as previously reported. The purified collagen was confirmed by SDS-PAGE and dialyzed against 20 mM tris−HCl buffer (pH 7.4). The lyophilized samples were stored at −20 °C for future use.

Synthesis of Zinc-Oxide Mesocrystals. A typical synthetic route of ZnO nanostructures is as follows. 297.5 mg of solid $Zn(NO_3)_2{\cdot}6H_2O$ (5.0 mmol) and 1 mL of 2 wt % collagen solution were added to 8 mL of water and stirred for 30 min to form a colorless transparent solution. 1 mL of 2 M NaOH aqueous solution was added to the mixture, and a white suspension was obtained. The final concentration of collagen and Zn(II) in the reaction system was estimated as 0.2 wt % and 0.1 M, respectively. The mixture was maintained at room temperature (~25 °C) for 8 days. White precipitates were harvested by centrifugation, washed with distilled water and ethanol in turn several times, and dried in air at room temperature. In order to investigate the effect of collagen on the morphology of the nanoparticles, the collagen concentration was varied from 0.01 to 0.5 wt % under a constant Zn(II) concentration of 0.1 M. In order to evaluate the role of Zn(II), the Zn(II) concentration was adjusted from 0.05 to 0.4 M, while the collagen concentration was kept as 0.2 wt %.

Characterization of Zinc-Oxide Mesocrystals. FESEM images of the precipitates were recorded using a Hitachi S-4800 field emission scanning electron microscope (Hitachi Limited, Japan) with an operating voltage of 5.0 kV. The samples were sputter-coated with Au for 25 s prior to imaging. TEM, HRTEM, SAED, and electron diffraction (EDX) measurements were carried out using a JEM-2100 transmission electron microscope (JEOL, Japan) at 200 kV. Powder XRD patterns were obtained on a Rigaku D/max-2400 X-ray diffractometer (Japan) with Cu Kα radiation (40 kV, 40 mA) at a scanning rate of 0.02°/s in the 2θ range from 10 to 80°. XPS experiments were performed on a Kratos Axis UltraDLD X-ray photoelectron spectrometer (England) with a monochrome X-ray source using AlKα (1486.6 eV) radiation. The measured binding energies were corrected by referencing the C 1s line to 284.5 eV. TGA was carried out on a TGA/NETZSCH STA449 F3 instrument under a nitrogen atmosphere at a heating rate of 10 °C/min from 27 °C to 800 °C. The Brunauer−Emmett−Teller (BET) method was employed to calculate the specific surface areas (S_{BET}). The room-temperature photoluminescence spectra were acquired on a Hitachi F-7000 luminescence spectrometer using a Xe lamp with an excitation wavelength of 325 nm. The UV−vis spectra of the ZnO samples were measured on a UV-1750 UV−vis spectrophotometer.

Photodegradation Performance of Zinc-Oxide Nanostructures. The photodegradation performance of the as-prepared zinc-oxide mesocrystals was evaluated using a broad

https://doi.org/10.1021/acsomega.1c04782
ACS Omega 2022, 7, 409−418

variety of organic dyes including RhB, rhodamine 6G, methylene blue, Coomassie brilliant blue R250, BPB, MO, Li Chunhong S, and carmine. The degradation of RhB was performed under ultraviolet light irradiation from a UV lamp (10 W). 10 mg of the ZnO sample was dispersed in 100 mL of RhB aqueous solution (12 mg/L). The suspension was stirred in the dark for 30 min before irradiation to achieve an adsorption−desorption equilibrium. The suspension was centrifuged at 8000 rpm for 5 min to remove the catalysts. The UV−vis absorption spectra of the supernatant were recorded using an Agilent UV-1750 spectrophotometer to monitor the concentration of RhB. The degradation of MO (12 mg/L) was performed under ultraviolet light irradiation following similar protocols. All other organic dyes (12 mg/L) were tested by exposure to sunlight for 2 days.

■ ASSOCIATED CONTENT

Supporting Information

The Supporting Information is available free of charge at https://pubs.acs.org/doi/10.1021/acsomega.1c04782.

XPS spectra of the zinc-oxide mesocrystals obtained after 8 days of collagen-templated biomineralization at room temperature ([collagen] = 0.2 wt %, [Zn (II)] = 0.1 M); survey spectrum; high-resolution Zn 2p spectrum; TGA curves of the as-prepared zinc-oxide mesocrystals obtained after 8 days via collagen-templated biomineralization at room temperature (black: [collagen] = 0.01 wt %, [Zn(II)] = 0.1 M; red: [collagen] = 0.2 wt %, [Zn^{2+}] = 0.1 mol/L); nitrogen adsorption/desorption isotherms of the apple-like zinc-oxide mesocrystals obtained after 8 days of collagen-templated biomineralization at room temperature ([collagen] = 0.2 wt %, [Zn(II)] = 0.1 M) and the corresponding BJH pore size distribution plot; FESEM images of the as-prepared zinc-oxide mesocrystals obtained after 8 days of biomineralization at room temperature with a constant concentration of collagen (0.2 wt %) and varying concentrations of zinc ions; degradation efficiency of RhB by various zinc-oxide nanostructures; and room-temperature photoluminescence spectra of the ZnO samples obtained after 8 days at room temperature with different collagen concentrations (PDF)

■ AUTHOR INFORMATION

Corresponding Author

Jianxi Xiao − *State Key Laboratory of Applied Organic Chemistry, Key Laboratory of Nonferrous Metal Chemistry and Resources Utilization of Gansu Province, College of Chemistry and Chemical Engineering, Lanzhou University, Lanzhou 730000, P. R. China*; orcid.org/0000-0002-9863-572X; Email: xiaojx@lzu.edu.cn

Authors

Huixia He − *State Key Laboratory of Applied Organic Chemistry, Key Laboratory of Nonferrous Metal Chemistry and Resources Utilization of Gansu Province, College of Chemistry and Chemical Engineering, Lanzhou University, Lanzhou 730000, P. R. China*

Caihong Fu − *State Key Laboratory of Applied Organic Chemistry, Key Laboratory of Nonferrous Metal Chemistry and Resources Utilization of Gansu Province, College of Chemistry and Chemical Engineering, Lanzhou University, Lanzhou 730000, P. R. China*

Wenyu Wei − *State Key Laboratory of Applied Organic Chemistry, Key Laboratory of Nonferrous Metal Chemistry and Resources Utilization of Gansu Province, College of Chemistry and Chemical Engineering, Lanzhou University, Lanzhou 730000, P. R. China*

Jianrui Ma − *State Key Laboratory of Applied Organic Chemistry, Key Laboratory of Nonferrous Metal Chemistry and Resources Utilization of Gansu Province, College of Chemistry and Chemical Engineering, Lanzhou University, Lanzhou 730000, P. R. China*

Xiaoyu Guo − *State Key Laboratory of Applied Organic Chemistry, Key Laboratory of Nonferrous Metal Chemistry and Resources Utilization of Gansu Province, College of Chemistry and Chemical Engineering, Lanzhou University, Lanzhou 730000, P. R. China*

Complete contact information is available at: https://pubs.acs.org/10.1021/acsomega.1c04782

Notes

The authors declare no competing financial interest.

■ ACKNOWLEDGMENTS

This work was supported by grants from the National Natural Science Foundation of China (grant nos. 22074057 and 21775059), the National Natural Science Foundation of Gansu Province (grant nos. 20YF3FA025 and 18YF1NA004), and the Lanzhou Talent Innovation and Entrepreneurship Project (grant no. 2019-RC-43).

■ REFERENCES

(1) Talarposhti, A. M.; Donnelly, T.; Anderson, G. K. Colour removal from a simulated dye wastewater using a two-phase Anaerobic packed bed reactor. *Water Res.* **2001**, *35*, 425−432.

(2) Lucas, M. S.; Dias, A. A.; Sampaio, A.; Amaral, C.; Peres, J. A. Degradation of a textile reactive Azo dye by a combined chemical-biological process: Fenton's reagent-yeast. *Water Res.* **2007**, *41*, 1103−1109.

(3) Dong, H.; Chen, G.; Sun, J.; Li, C.; Yu, Y.; Chen, D. A novel high-efficiency visible-light sensitive Ag2CO3 photocatalyst with universal photodegradation performances: Simple synthesis, reaction mechanism and first-principles study. *Appl. Catal., B* **2013**, *134−135*, 46−54.

(4) Yagub, M. T.; Sen, T. K.; Afroze, S.; Ang, H. M. Dye and its removal from aqueous solution by adsorption: A review. *Adv. Colloid Interface Sci.* **2014**, *209*, 172−184.

(5) Liu, B.; Guo, W. Q.; Ren, N. Q. Decontamination of Wastewaters Containing Synthetic Organic Dyes by Electrochemical Methods: A Review. *Adv. Mater. Res.* **2013**, *788*, 405−408.

(6) León, O.; Muñoz-Bonilla, A.; Soto, D.; Pérez, D.; Rangel, M.; Colina, M.; Fernández-García, M. Removal of anionic and cationic dyes with bioadsorbent oxidized chitosans. *Carbohydr. Polym.* **2018**, *194*, 375−383.

(7) Liu, X.; Tian, J.; Li, Y.; Sun, N.; Mi, S.; Xie, Y.; Chen, Z. Enhanced dyes adsorption from wastewater via Fe3O4 nanoparticles functionalized activated carbon. *J. Hazard. Mater.* **2019**, *373*, 397−407.

(8) Xiao, W.; Garba, Z. N.; Sun, S.; Lawan, I.; Wang, L.; Lin, M.; Yuan, Z. Preparation and evaluation of an effective activated carbon from white sugar for the adsorption of rhodamine B dye. *J. Cleaner Prod.* **2020**, *253*, 119989−120026.

(9) Gupta, V. K.; Suhas. Application of low-cost adsorbents for dye removal - A review. *J. Environ. Manage.* **2009**, *90*, 2313−2342.

(10) Brillas, E.; Martínez-Huitle, C. A. Decontamination of wastewaters containing synthetic organic dyes by electrochemical methods. An updated review. *Appl. Catal., B* **2015**, *166*−*167*, 603.
(11) Trellu, C.; Mousset, E.; Pechaud, Y.; Huguenot, D.; van Hullebusch, E. D.; Esposito, G.; Oturan, M. A. Removal of hydrophobic organic pollutants from soil washing/flushing solutions: A critical review. *J. Hazard. Mater.* **2016**, *306*, 149−174.
(12) Liu, M.; Yin, W.; Zhao, T.-L.; Yao, Q.-Z.; Fu, S.-Q.; Zhou, G.-T. High-efficient removal of organic dyes from model wastewater using Mg(OH)2-MnO2 nanocomposite: Synergistic effects of adsorption, precipitation, and photodegradation. *Sep. Purif. Technol.* **2021**, *272*, 118901−118910.
(13) Xiao, W.; Jiang, X.; Liu, X.; Zhou, W.; Garba, Z. N.; Lawan, I.; Wang, L.; Yuan, Z. Adsorption of organic dyes from wastewater by metal-doped porous carbon materials. *J. Cleaner Prod.* **2021**, *284*, 124773−124793.
(14) Kuo, W. S.; Ho, P. H. Solar photocatalytic decolorization of methylene blue in water. *Chemosphere* **2001**, *45*, 77−83.
(15) Labanda, J.; Sabate, J.; Llorens, J. Modeling of the dynamic adsorption of an anionic dye through ion-exchange membrane adsorber. *J. Membr. Sci.* **2009**, *340*, 234−240.
(16) Anushree, C.; Philip, J. Efficient removal of methylene blue dye using cellulose capped Fe3O4 nanofluids prepared using oxidation-precipitation method. *Colloids Surf., A* **2019**, *567*, 193−204.
(17) Chang, F.; Wang, J.; Luo, J.; Sun, J.; Hu, X. Synthesis, characterization, and visible-light-driven photocatalytic performance of W-SBA15. *J. Colloid Interface Sci.* **2016**, *468*, 284−291.
(18) He, R.-A.; Cao, S. W.; Jia-Guo, Y. U. Recent Advances in Morphology Control and Surface Modification of Bi-Based Photocatalysts. *Acta Phys.-Chim. Sin.* **2016**, *32*, 2841−2870.
(19) Low, J.; Yu, J.; Jaroniec, M.; Wageh, S.; Al-Ghamdi, A. A. Heterojunction Photocatalysts. *Adv. Mater.* **2017**, *29*, 1601694−1601714.
(20) Kuang, P.-Y.; Su, Y.-Z.; Xiao, K.; Liu, Z.-Q.; Li, N.; Wang, H.-J.; Zhang, J. Double-Shelled CdS- and CdSe-Cosensitized ZnO Porous Nanotube Arrays for Superior Photoelectrocatalytic Applications. *ACS Appl. Mater. Interfaces* **2015**, *7*, 16387−16394.
(21) Liu, D.; Wu, Z.; Tian, F.; Ye, B.-C.; Tong, Y. Synthesis of N and La co-doped TiO2/AC photocatalyst by microwave irradiation for the photocatalytic degradation of naphthalene. *J. Alloys Compd.* **2016**, *676*, 489−498.
(22) Vázquez, A.; Hernández-Uresti, D. B.; Obregón, S. Electrophoretic deposition of CdS coatings and their photocatalytic activities in the degradation of tetracycline antibiotic. *Appl. Surf. Sci.* **2016**, *386*, 412−417.
(23) Liu, Y.; Yu, L.; Hu, Y.; Guo, C.; Zhang, F.; Wen Lou, X. A magnetically separable photocatalyst based on nest-like γ-Fe2O3/ZnO double-shelled hollow structures with enhanced photocatalytic activity. *Nanoscale* **2012**, *4*, 183−187.
(24) Yu, J.; Yu, X. Hydrothermal synthesis and photocatalytic activity of zinc oxide hollow spheres. *Environ. Sci. Technol.* **2008**, *42*, 4902−4907.
(25) Shekofteh-Gohari, M.; Habibi-Yangjeh, A. Fabrication of novel magnetically separable visible-light-driven photocatalysts through photosensitization of Fe 3 O 4 /ZnO with CuWO 4. *J. Ind. Eng. Chem.* **2016**, *44*, 174−184.
(26) Kumar, S. G.; Rao, K. S. R. K. Comparison of modification strategies towards enhanced charge carrier separation and photocatalytic degradation activity of metal oxide semiconductors (TiO 2 , WO 3 and ZnO). *Appl. Surf. Sci.* **2017**, *391*, 124−148.
(27) Huang, N.; Shu, J.; Wang, Z.; Chen, M.; Ren, C.; Zhang, W. One-step pyrolytic synthesis of ZnO nanorods with enhanced photocatalytic activity and high photostability under visible light and UV light irradiation. *J. Alloys Compd.* **2015**, *648*, 919−929.
(28) Turchi, C.; Ollis, D. F. Photocatalytic degradation of organic water contaminants: Mechanisms involving hydroxyl radical attack. *J. Catal.* **1990**, *122*, 178−192.
(29) Hoffmann, M. R.; Martin, S. T.; Choi, W.; Bahnemann, D. W. Environmental Applications of Semiconductor Photocatalysis. *Chem. Rev.* **1995**, *95*, 69−96.
(30) Pal, B.; Sharon, M. Enhanced photocatalytic activity of highly porous ZnO thin films prepared by sol-gel process. *Mater. Chem. Phys.* **2002**, *76*, 82−87.
(31) Daneshvar, N.; Salari, D.; Khataee, A. R. Photocatalytic degradation of azo dye acid red 14 in water on ZnO as an alternative catalyst to TiO 2. *J. Photochem. Photobiol., A* **2004**, *162*, 317−322.
(32) Senapati, S.; Srivastava, S. K.; Singh, S. B. Synthesis, characterization and photocatalytic activity of magnetically separable hexagonal Ni/ZnO nanostructure. *Nanoscale* **2012**, *4*, 6604−6612.
(33) Jin, X.; Coetz, M.; Wille, S.; Mishra, Y. K.; Adelung, R.; Zollfrank, C. A Novel Concept for Self-Reporting Materials: Stress Sensitive Photoluminescence in ZnO Tetrapod Filled Elastomers. *Adv. Mater.* **2013**, *25*, 1342−1347.
(34) Reimer, T.; Paulowicz, I.; Röder, R.; Kaps, S.; Lupan, O.; Chemnitz, S.; Benecke, W.; Ronning, C.; Adelung, R.; Mishra, Y. K. Single step integration of ZnO nano- and microneedles in Si trenches by novel flame transport approach: whispering gallery modes and photocatalytic properties. *ACS Appl. Mater. Interfaces* **2014**, *6*, 7806−7815.
(35) Ansari, S. A.; Khan, M. M.; Ansari, M. O.; Lee, J.; Cho, M. H. Biogenic Synthesis, Photocatalytic, and Photoelectrochemical Performance of Ag-ZnO Nanocomposite. *J. Phys. Chem. C* **2013**, *117*, 27023−27030.
(36) Lee, H. J.; Kim, J. H.; Park, S. S.; Hong, S. S.; Lee, G. D. Degradation kinetics for photocatalytic reaction of methyl orange over Al-doped ZnO nanoparticles. *J. Ind. Eng. Chem.* **2015**, *25*, 199−206.
(37) Xie, R.; Li, D.; Zhang, H.; Yang, D.; Jiang, M.; Sekiguchi, T.; Liu, B.; Bando, Y. Low-temperature growth of uniform ZnO particles with controllable ellipsoidal morphologies and characteristic luminescence patterns. *J. Phys. Chem. B* **2006**, *110*, 19147−19153.
(38) Zhou, X.; Zhang, D.; Zhu, Y.; Shen, Y.; Guo, X.; Ding, W.; Chen, Y. Mechanistic investigations of PEG-directed assembly of one-dimensional ZnO nanostructures. *J. Phys. Chem. B* **2006**, *110*, 25734−25739.
(39) Gao, Y.; Li, A. D.; Gu, Z. B.; Wang, Q. J.; Zhang, Y.; Wu, D.; Chen, Y. F.; Ming, N. B.; Ouyang, S. X.; Yu, T. Fabrication and optical properties of two-dimensional ZnO hollow half-shell arrays. *Appl. Phys. Lett.* **2007**, *91*, 031910−031913.
(40) Feng, J.-J.; Liao, Q.-C.; Wang, A.-J.; Chen, J.-R. Mannite supported hydrothermal synthesis of hollow flower-like ZnO structures for photocatalytic applications. *Crystengcomm* **2011**, *13*, 4202−4210.
(41) Wang, A.-J.; Liao, Q.-C.; Feng, J.-J.; Zhang, P.-P.; Li, A.-Q.; Wang, J.-J. Apple pectin-mediated green synthesis of hollow double-caged peanut-like ZnO hierarchical superstructures and photocatalytic applications. *CrystEngComm* **2012**, *14*, 256−263.
(42) Wang, J.; Hou, S.; Zhang, L.; Chen, J.; Xiang, L. Ultra-rapid formation of ZnO hierarchical structures from dilution-induced supersaturated solutions. *Crystengcomm* **2014**, *16*, 7115−7123.
(43) Rokade, A.; Rondiya, S.; Gabhale, B.; Diwate, K.; Karpe, S.; Mayabadi, A.; Pandharkar, S.; Sharma, V.; Lonkar, G.; Pathan, H.; Jadkar, S. Electrodeposition of template free hierarchical ZnO nanorod arrays via a chloride medium. *J. Mater. Sci.: Mater. Electron.* **2016**, *27*, 12357−12364.
(44) Singh, A.; Kumar, D.; Khanna, P. K.; Kumar, M. Reduction in point defects of sol-gel derived ZnO thin films with oxygen ambient. *Mater. Lett.* **2016**, *183*, 365−368.
(45) Sun, Y.; Guo, H.; Zhang, W.; Zhou, T.; Qiu, Y.; Xu, K.; Zhang, B.; Yang, H. Synthesis and characterization of twinned flower-like ZnO structures grown by hydrothermal methods. *Ceram. Int.* **2016**, *42*, 9648−9652.
(46) Qian, C.; Yin, J. J.; Zhao, J. X.; Li, X. T.; Wang, S. F.; Bai, Z. H.; Jiao, T. F. Facile preparation and highly efficient photodegradation performances of self-assembled Artemia eggshell-ZnO nanocomposites for wastewater treatment. *Colloids Surf., A* **2021**, *610*, 125752.

https://doi.org/10.1021/acsomega.1c04782
ACS Omega 2022, 7, 409−418

(47) Fang, J.; Fan, H.; Ma, Y.; Wang, Z.; Chang, Q. Surface defects control for ZnO nanorods synthesized by quenching and their anti-recombination in photocatalysis. *Appl. Surf. Sci.* **2015**, *332*, 47−54.
(48) Zimmermann, E. A.; Ritchie, R. O. Bone as a Structural Material. *Adv. Healthcare Mater.* **2015**, *4*, 1287−1304.
(49) Tertuliano, O. A.; Greer, J. R. The nanocomposite nature of bone drives its strength and damage resistance. *Nat. Mater.* **2016**, *15*, 1195−1202.
(50) Ong, B. S.; Li, C.; Li, Y.; Wu, Y.; Loutfy, R. Stable, solution-processed, high-mobility ZnO thin-film transistors. *J. Am. Chem. Soc.* **2007**, *129*, 2750−2751.
(51) Ameen, S.; Akhtar, M. S.; Seo, H.-K.; Kim, Y. S.; Shin, H. S. Influence of Sn doping on ZnO nanostructures from nanoparticles to spindle shape and their photoelectrochemical properties for dye sensitized solar cells. *Chem. Eng. J.* **2012**, *187*, 351−356.
(52) Yang, Y.; Yang, Y.; Wu, H.; Guo, S. Control of the formation of rod-like ZnO mesocrystals and their photocatalytic properties. *Crystengcomm* **2013**, *15*, 2608−2615.
(53) Liang, S.; Gou, X.; Cui, J.; Luo, Y.; Qu, H.; Zhang, T.; Yang, Z.; Yang, Q.; Sun, S. Novel cone-like ZnO mesocrystals with co-exposed $(10\bar{1}1)$ and $(000\bar{1})$ facets and enhanced photocatalytic activity. *Inorg. Chem. Front.* **2018**, *5*, 2257−2267.
(54) Sun, S.; Zhang, X.; Yu, X.; Cui, J.; Yang, M.; Yang, Q.; Xiao, P.; Liang, S. Unprecedented Ag-Cu2O composited mesocrystals with efficient charge separation and transfer as well as visible light harvesting for enhanced photocatalytic activity. *Nanoscale* **2021**, *13*, 11867−11877.
(55) Sun, S.; Yu, X.; Yang, Q.; Yang, Z.; Liang, S. Mesocrystals for photocatalysis: a comprehensive review on synthesis engineering and functional modifications. *Nanoscale Adv.* **2019**, *1*, 34−63.
(56) Yoshizumi, A.; Yu, Z.; Silva, T.; Thiagarajan, G.; Ramshaw, J. A. M.; Inouye, M.; Brodsky, B. Self-association ofstreptococcus pyogenescollagen-like constructs into higher order structures. *Protein Sci.* **2009**, *18*, 1241−1251.

https://doi.org/10.1021/acsomega.1c04782
ACS Omega 2022, 7, 409−418